The Astrophysical Journal Letters, 928:L3 (17pp), 2022 March 20 https://doi.org/10.3847/2041-8213/ac5a56


# The Two Hot Corinos of the SVS13-A Protostellar Binary System: Counterposed Siblings

Eleonora Bianchi[1], Ana López-Sepulcre[1,2], Cecilia Ceccarelli[1], Claudio Codella[3,1], Linda Podio[3], Mathilde Bouvier[1], and Joan Enrique-Romero[1,4]
[1] Univ. Grenoble Alpes, CNRS, IPAG, F-38000 Grenoble, France; eleonora.bianchi@univ-grenoble-alpes.fr
[2] Institut de Radioastronomie Millimétrique, 38406 Saint-Martin d' Hères, France
[3] INAF, Osservatorio Astrofisico di Arcetri, Largo E. Fermi 5, I-50125, Firenze, Italy
[4] Departament de Química, Universitat Autònoma de Barcelona, Bellaterra, E-08193, Catalonia, Spain
*Received 2021 November 24; revised 2022 March 3; accepted 2022 March 3; published 2022 March 21*

## Abstract

We present ALMA high-angular-resolution (∼50 au) observations of the Class I binary system SVS13-A. We report images of SVS13-A in numerous interstellar complex organic molecules: $CH_3OH$, $^{13}CH_3OH$, $CH_3CHO$, $CH_3OCH_3$, and $NH_2CHO$. Two hot corinos at different velocities are imaged in VLA4A ($V_{sys} = +7.7\,km\,s^{-1}$) and VLA4B ($V_{sys} = +8.5\,km\,s^{-1}$). From a non-LTE analysis of methanol lines, we derive a gas density of $3 \times 10^8\,cm^{-3}$ and gas temperatures of 140 and 170 K for VLA4A and VLA4B, respectively. For the other species, the column densities are derived from an LTE analysis. Formamide, which is the only N-bearing species detected in our observations, is more prominent around VLA4A, while dimethyl ether, methanol, and acetaldehyde are associated with both VLA4A and VLA4B. We derive in the two hot corinos abundance ratios of ∼1 for $CH_3OH$, $^{13}CH_3OH$, and $CH_3OCH_3$; ∼2 for $CH_3CHO$; and ∼4 for $NH_2CHO$. The present data set supports chemical segregation between the different species inside the binary system. The emerging picture is that of an onion-like structure of the two SVS13-A hot corinos, caused by the different binding energies of the species, also supported by ad hoc quantum chemistry calculations. In addition, the comparison between molecular and dust maps suggests that the interstellar complex organic molecules emission originates from slow shocks produced by accretion streamers impacting the VLA4A and VLA4B disks and enriching the gas-phase component.

*Unified Astronomy Thesaurus concepts:* Astrochemistry (75)

## 1. Introduction

The birth of planets inside protostellar disks has been traced back in time, as a result of recent ALMA high-angular-resolution observations showing substructures in the dust distribution of young (<1 Myr) disks, which may be caused by the interaction of the disk material with forming planets (Sheehan & Eisner 2017; Segura-Cox et al. 2020; Sheehan et al. 2020). Protostellar Class 0/I disks are thus the ideal environment to investigate the initial conditions and the chemical content, which will be at least partially inherited by forming planets (e.g., Öberg & Bergin 2021). From a chemical point of view, close binaries are unique laboratories as they are expected to originate from the same parent core, i.e., the same initial gas composition and similar gas conditions, in terms of temperature, density, and UV illumination. Observed differences in the chemistry of the two binary components are then expected to be the result of a chemical evolution inside the system (e.g., Manigand et al. 2020). SVS13-A is a perfect case study because it is a very well-studied Class I protostellar system in NGC 1333, hosting a rich chemistry including emission from several interstellar complex organic molecules (hereafter iCOMs; López-Sepulcre et al. 2015; Codella et al. 2016; Bianchi et al. 2017; De Simone et al. 2017; Bianchi et al. 2019; Belloche et al. 2020; Diaz-Rodriguez et al. 2021; Yang et al. 2021). The two components of the binary system (VLA4A and VLA4B) have a separation of ∼0.″3 (∼90 au at the source distance of 299 pc), and they have been imaged in the continuum using ALMA (Tobin et al. 2016, 2018; Diaz-Rodriguez et al. 2021). Recently, the presence of two hot corinos in both VLA4A and VLA4B has been reported by Diaz-Rodriguez et al. (2021). The detection of ethylene glycol only toward VLA4A suggests the possibility of different chemistry at work in the two binaries, calling for mapping different iCOMs using different excitation transitions. In this Letter, we present ALMA high-angular-resolution observations, imaging the SVS13-A binary system using a large number of lines (17) due to both O-bearing and N-bearing iCOMs, namely methanol ($CH_3OH$ and $^{13}CH_3OH$), acetaldehyde ($CH_3CHO$), dimethyl ether ($CH_3OCH_3$), and formamide ($NH_2CHO$), down to planet-formation scales.

## 2. Observations

The system SVS13-A was observed with ALMA (2018.1.01461.S) in Band 6. Data were acquired on 2019 September 8 using the C43-6 configuration, with baselines between 43 m and 5.9 km. The observations were centered at $\alpha_{J2000} = 03^h29^m3.^s8$, $\delta_{J2000} = +31°16'03.''8$. The quasar J0510 +1800 was used as bandpass and flux calibrator, while J0336 +3218 was the phase calibrator. The absolute flux calibration uncertainty is 20%. Data were calibrated using the standard ALMA calibration pipeline within CASA (McMullin et al. 2007). Phase self-calibration has been performed using the IRAM-GILDAS[5] package, after the determination of line-free continuum channels, and the solutions applied to both the continuum and spectral cubes. The observed spectral windows, as well as the synthesized beam and the rms noise of the



[5] http://www.iram.fr/IRAMFR/GILDAS

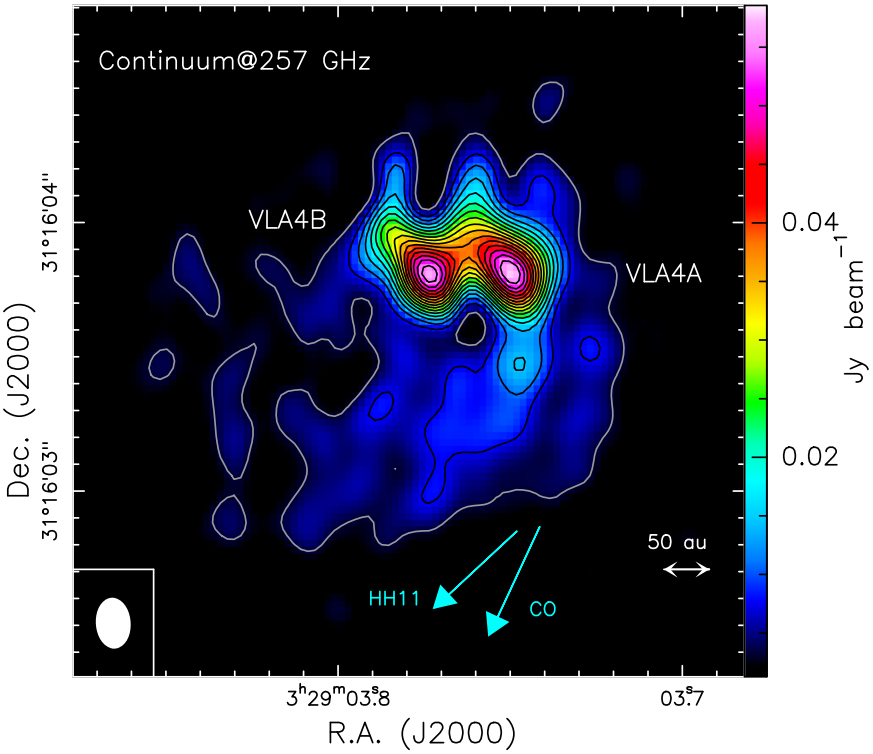


**Figure 1.** Dust continuum emission at 257 GHz as observed by ALMA (color scale and contours). First contours (gray) and steps (black) are $8\sigma$, corresponding to 3.35 mJy beam$^{-1}$. The beam size is $0\farcs19 \times 0\farcs13$ (PA $= +5°$). The binary system is composed of VLA4A (right) and VLA4B (left). Coordinates are $\alpha_{J2000} = 03^h\ 29^m\ 3\fs75$, $\delta_{J2000} = +31°16'03\farcs81$ and $\alpha_{J2000} = 03^h\ 29^m\ 3\fs773$, $\delta_{J2000} = +31°16'03\farcs81$ for VLA4A and VLA4B, respectively. The blue arrows indicate the directions toward HH 11 (133°) as well as the main axis of the $H_2$/CO jet (155°) as inferred by Lefèvre et al. (2017).

continuum-subtracted line cubes, using spectral channels of 122 kHz (0.15 km s$^{-1}$), are reported in Table B1.

## 3. Results

### 3.1. Continuum Emission

Figure 1 shows the SVS13-A map of the dust continuum emission at 1.3 mm. The two emission peaks correspond to the two components of the SVS13-A system previously observed with ALMA as well as at centimeter wavelengths (Carrasco-González et al. 2008; Tobin et al. 2018; Diaz-Rodriguez et al. 2021): VLA4A and VLA4B. In addition, the map shows arc-like structures in agreement with that observed by Tobin et al. (2016, 2018) and Diaz-Rodriguez et al. (2021): a bright arc (up to $32\sigma$) extending from the southern edge of the continuum associated with VLA4A toward the southeast and two fainter arcs (up to $16\sigma$) parallel to the first one and extending on the east (i.e., from the southern edge of the continuum associated with VLA4B) and on the west side of VLA4A. In addition, the present image shows further three elongated structures extending from the northern edge of the continuum associated with VLA4A and B toward the north, with a slightly negative PA. As the ALMA beam is roughly elongated along the N–S direction (PA $= +5°$), we checked for the presence of possible artifacts caused by the cleaning process by repeating the cleaning using different tapering. With a larger circular beam, all the elongated arc-like structures, including the three structures toward the north, are less evident but still present. The presence of accretion streamers, suggested for VLA4B (Diaz-Rodriguez et al. 2021), is then confirmed by the present ALMA data set also toward VLA4A, and it has an impact on the following discussion on the origin of iCOM emission (Section 5.1).

The continuum emission associated with VLA4A and VLA4B has a disk-like structure. We modeled the continuum emission in the *uv* plane assuming two elliptical inclined disks centered on the continuum peak positions. The best fitting is obtained with one disk with axes $0\farcs602$ ($0\farcs001$) $\times$ $0\farcs231$ ($0\farcs077$) and PA 41.1° (0°.1) centered toward VLA4A and a second disk with axes $0\farcs325$ ($0\farcs242$) $\times$ $0\farcs205$ ($0\farcs153$) and PA 33°.8 (0°.1) centered toward VLA4B. The integrated fluxes are 183.15 (0.87) mJy and 126.06 (0.55) mJy for VLA4A and VLA4B, respectively. The sizes are $\sim$180 $\times$ 70 au (VLA4A) and 90 $\times$ 70 au (VLA4B). From the axis ratio, we can infer an inclination of 67° and 51° (with respect to the plane of the sky) for the VLA4A and VLA4B disks, respectively. We calculate the disk masses assuming isothermal and optically thin dust emission. If we assume a dust temperature of 140 K, as derived from line analysis, a dust-to-gas ratio of 1/100, and a dust mass opacity coefficient $k_\nu$ of 1.0 cm$^2$ g$^{-1}$ (Ossenkopf & Henning 1994), we obtain 0.029 $M_\odot$ for VLA4A and 0.020 $M_\odot$ for VLA4B. The value obtained for VLA4B is consistent with that reported by Diaz-Rodriguez et al. (2021), while the one for VLA4A is higher by a factor of 3. If we assume a lower dust temperature of 30 K, we obtain 0.159 $M_\odot$ for VLA4A and 0.110 $M_\odot$ for VLA4B, in good agreement with that found by Tobin et al. (2018).

### 3.2. Emission from iCOMs

We detected a total of 17 emission lines from 4 iCOMs (Table 1). More specifically, we detected four lines of $CH_3OH$ and five lines of $^{13}CH_3OH$, covering upper-level energies ($E_{up}$)

**Table 1**
Properties of the Lines Detected toward SVS13-A

| Transition | $\nu$[a] (GHz) | $E_{up}$[a] (K) | $S\mu^2$[a] ($D^2$) | $I_{int}$[b] (K km $s^{-1}$) | | |
|---|---|---|---|---|---|---|
| | | | | VLA4A | VLA4B | VLA4A/VLA4B |
| $CH_3OH$ $25_{3,22}$–$25_{2,23}$ A | 241.588758 | 804 | 102 | 251 (53) | 112 (26) | 2.2 (0.7) |
| $CH_3OH$ $5_{2,3}$–$4_{2,2}$ E | 241.904147 | 61 | 14 | 454 (95) | 353 (74) | 1.3 (0.4) |
| $CH_3OH$ $5_{-2,4}$–$4_{-2,3}$ E | 241.904643 | 57 | 13 | | | |
| $CH_3OH$ $16_{3,14}$–$16_{2,15}$ A | 255.241888 | 365 | 59 | 410 (86) | 267 (56) | 1.5 (0.5) |
| $^{13}CH_3OH$ $4_{3,2}$–$4_{2,3}$ A | 255.203728 | 73 | 3 | 138 (31) | 102 (23) | 1.4 (0.4) |
| $^{13}CH_3OH$ $3_{3,0}$–$3_{2,1}$ A | 255.210605 | 64 | 2 | 110 (25) | 76 (18) | |
| $^{13}CH_3OH$ $7_{3,5}$–$7_{2,6}$ A | 255.214891 | 113 | 6 | 195 (42) | 148 (32) | |
| $^{13}CH_3OH$ $3_{3,1}$–$3_{2,2}$ A[c] | 255.220865 | 64 | 2 | <118 | <80 | |
| $^{13}CH_3OH$ $14_{3,12}$–$14_{2,13}$ A | 256.826572 | 288 | 13 | 147 (32) | 91 (21) | 1.6 (0.5) |
| $CH_3CHO$ $13_{1,13}$–$12_{1,12}$ E | 242.106020 | 84 | 163 | 161 (35) | 66 (16) | 2.4 (0.8) |
| $CH_3CHO$ $13_{1,13}$–$12_{1,12}$ A | 242.118136 | 84 | 163 | 155 (35) | 48 (13) | 3.2 (1.1) |
| $CH_3OCH_3$ $5_{3,2}$–$4_{2,3}$ AE | 241.523808 | 26 | 28 | >51[d] | >41[d] | |
| $CH_3OCH_3$ $5_{3,2}$–$4_{2,3}$ EA | 241.528318 | | 15 | | | |
| $CH_3OCH_3$ $5_{3,2}$–$4_{2,3}$ EE | 241.528719 | | 69 | | | |
| $CH_3OCH_3$ $5_{3,2}$–$4_{2,3}$ AA | 241.531026 | | 46 | | | |
| $CH_3OCH_3$ $21_{3,18}$–$20_{4,17}$ AA | 241.635773 | 226 | 61 | <58[e] | <60[e] | |
| $CH_3OCH_3$ $21_{3,18}$–$20_{4,17}$ EE | 241.637303 | | 97 | | | |
| $CH_3OCH_3$ $21_{3,18}$–$20_{4,17}$ AE | 241.638831 | | 37 | | | |
| $CH_3OCH_3$ $21_{3,18}$–$20_{4,17}$ EA | 241.638834 | | 24 | | | |
| $CH_3OCH_3$ $13_{1,13}$–$12_{0,12}$ EA | 241.946249 | 81 | 34 | 131 (29) | 136 (30) | 1.0 (0.3) |
| $CH_3OCH_3$ $13_{1,13}$–$12_{0,12}$ AE | 241.946249 | | 69 | | | |
| $CH_3OCH_3$ $13_{1,13}$–$12_{0,12}$ EE | 241.946542 | | 274 | | | |
| $CH_3OCH_3$ $13_{1,13}$–$12_{0,12}$ AA | 241.946835 | | 103 | | | |
| $CH_3OCH_3$ $19_{5,14}$–$19_{4,15}$ AE | 256.135096 | 208 | 104 | 106 (25) | 117 (27) | 0.9 (0.3) |
| $CH_3OCH_3$ $19_{5,14}$–$19_{4,15}$ EA | 256.135164 | | 69 | | | |
| $CH_3OCH_3$ $19_{5,14}$–$19_{4,15}$ EE | 256.137180 | | 278 | | | |
| $CH_3OCH_3$ $19_{5,14}$–$19_{4,15}$ AA | 256.139230 | | 174 | | | |
| $NH_2CHO$ $12_{1,12}$–$11_{1,11}$ | 243.521044 | 79 | 156 | 267 (59) | 40 (11) | 7 (2) |
| $NH_2CHO$ $12_{4,9}$–$11_{4,8}$ | 255.058533 | 127 | 139 | 160 (37) | 42 (12) | 4 (1) |
| $NH_2CHO$ $12_{4,8}$–$11_{4,7}$ | 255.078912 | 127 | 139 | >93[f] | >39[f] | |

**Notes.**
[a] Frequencies and spectroscopic parameters have been provided by (Kukolich & Nelson 1971; Xu & Lovas 1997; Xu et al. 2008; Endres et al. 2009, and references therein) for $CH_3OH$, $^{13}CH_3OH$, $CH_3OCH_3$, and $NH_2CHO$, respectively, and retrieved from the Cologne Database for Molecular Spectroscopy, http://www.astro.uni-koeln.de/cdms/ (Müller et al. 2005). They were provided by Kleiner et al. (1996) and retrieved from the Jet Propulsion Laboratory molecular database, https://spec.jpl.nasa.gov/ (Pickett et al. 1998) for $CH_3CHO$.
[b] Errors on the integrated intensity include 20% of calibration.
[c] Contaminated by the $NH_2CHO$ $123,10$–$11_{3,9}$ line at 255.225651 GHz.
[d] The line profile is truncated as the line is close to the edge of the spectral window.
[e] Tentatively detected (line peak below 3σ detection limit).
[f] The $NH_2CHO$ $12_{3,10}$–$11_{3,9}$ line at 255.225651 GHz is also detected but not considered for the analysis as strongly contaminated by $^{13}CH_3OH$ (see c).

from 57 K to 804 K. We also detected two $CH_3CHO$ lines (84 K), four lines of $CH_3OCH_3$ (26–226 K), and three lines of $NH_2CHO$ (79–127 K). In Figure 2, we show the emission of one representative line for each species, integrated on three velocity intervals, namely the $CH_3OH$ $25_{3,22}$–$25_{2,23}$ A at 241.589 GHz; the $^{13}CH_3OH$ $14_{3,12}$–$14_{2,13}$ A line at 256.827 GHz; the $CH_3CHO$ $13_{1,13}$–$12_{1,12}$ E line at 242.106 GHz; the $13_{1,13}$–$12_{0,12}$ EA, AE, EE, and AA transitions at 241.946 GHz; and the $NH_2CHO$ $12_{4,9}$–$11_{4,8}$ transition at 255.059 GHz. The lines are representative of each species, independently of their upper-level energy. All the maps are reported in Figures C1–C5. Figure 2 also shows the iCOM spectra extracted in the positions corresponding to the continuum peak position of the two sources VLA4A and VLA4B. From the $^{13}CH_3OH$ spectra, we reveal different systemic velocities for VLA4A (+7.7 km $s^{-1}$) and VLA4B (+8.5 km $s^{-1}$). The spatial distribution of iCOMs is different for the different species. For $CH_3OH$ and $^{13}CH_3OH$, in the interval between +4.0 and +7.5 km $s^{-1}$, the line emission traces VLA4A, with an elongation toward the north. In the velocity intervals 7.5–8.7 km $s^{-1}$, corresponding to the systemic velocity reported for SVS13-A, and 8.8–12.0 km $s^{-1}$, the line emission is associated with both protostars, peaking in between. A beam deconvolved size of $0\farcs6 \times 0\farcs4$ is derived from a simple 2D Gaussian fit in the image plane of the $^{13}CH_3OH$ moment 0 emission. For $CH_3OCH_3$, the spatial distribution is similar but the emission between +8.8 and +11 km $s^{-1}$ peaks closer to VLA4B. Acetaldehyde emission between 8.8 and 11 km $s^{-1}$ peaks closer to VLA4A. Finally, formamide, which is the only N-bearing species detected in our observations, is peaking toward VLA4A.

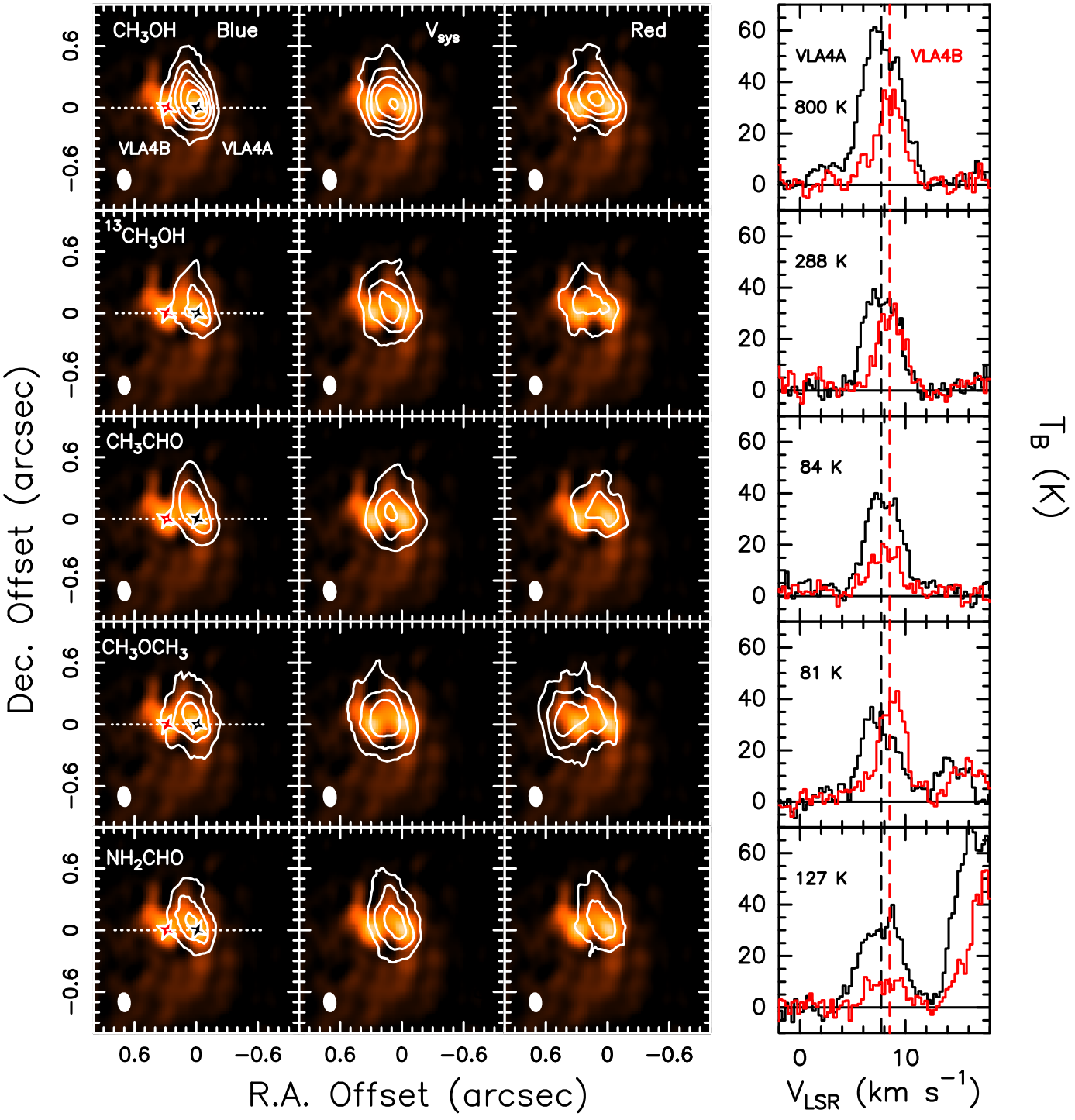


**Figure 2.** Integrated emission from $CH_3OH$, $^{13}CH_3OH$, $CH_3CHO$, $NH_2CHO$, and $CH_3OCH_3$, in white contours, superposed to the dust emission in color scale. The emission is integrated in the following velocity intervals: 4–7.5 km s$^{-1}$ in the left panels ($V_{sys}$ − ), 7.5–8.7 km s$^{-1}$ in the middle panels ($V_{sys}$), and 8.8–12.0 km s$^{-1}$ in the right panels ($V_{sys}$ + ). The first contours and steps are 5$\sigma$, corresponding to 35 mJy beam$^{-1}$, 19 mJy beam$^{-1}$ and 29 mJy beam$^{-1}$, for $CH_3OH$; 34 mJy beam$^{-1}$, 21 mJy beam$^{-1}$ and 28 mJy beam$^{-1}$ for $^{13}CH_3OH$; 29 mJy beam$^{-1}$, 19 mJy beam$^{-1}$ and 26 mJy beam$^{-1}$ for $CH_3CHO$; 30 mJy beam$^{-1}$, 18 mJy beam$^{-1}$ and 29 mJy beam$^{-1}$ for $CH_3OCH_3$; and 33 mJy beam$^{-1}$, 24 mJy beam$^{-1}$, and 27 mJy beam$^{-1}$ for $NH_2CHO$, respectively. The synthesized beams are reported in white in the lower-left corner of each panel. The dashed line indicates the axes connecting VLA4A and VLA4B along which the line intensity profiles shown in Figure 3 are extracted. On the right, we report the spectra in brightness temperature units, extracted at the continuum peak position of VLA4A (black star) and VLA4B (red star). From $^{13}CH_3OH$ spectra, we derived a systemic velocity of +7.7 km s$^{-1}$ for VLA4A (black vertical dashed line) and +8.5 km s$^{-1}$ for VLA4B (red vertical dashed line). Spectra are smoothed at 0.3 km s$^{-1}$ resolution. On the left is reported the upper-level energy of each transition in K.

In Table 1 we report the integrated line intensities extracted from the continuum peak positions of VLA4A and VLA4B, respectively, and their intensity ratios. The intensity ratios are close to the value of 1 for $CH_3OCH_3$, confirming that dimethyl ether is present in both protostars. For methanol and acetaldehyde, intensity ratios vary from 1.3 to 3.2, while formamide abundances are higher in VLA4A by factors of 4–7. The intensity ratios suggest chemical differentiation inside the system. To further

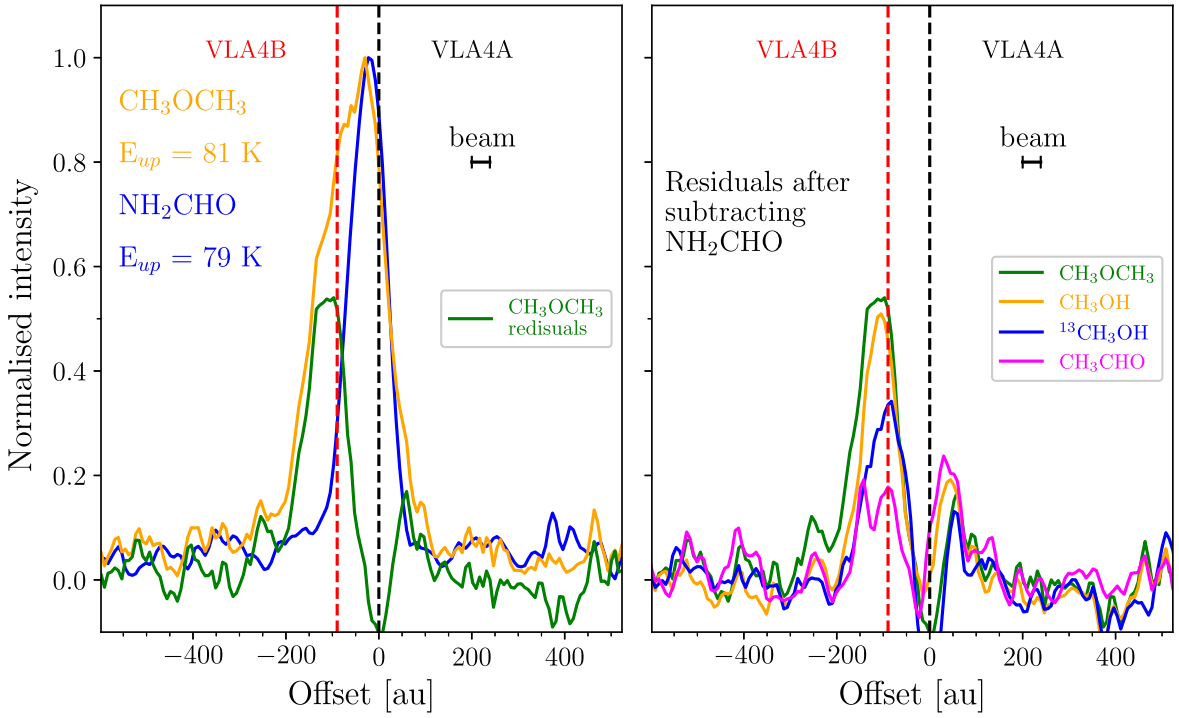


**Figure 3.** Left panel: normalized intensity profile of the $NH_2CHO$ line at 243.521 GHz (blue) and the $CH_3OCH_3$ line at 241.946 GHz (orange) extracted along the line connecting VLA4A with VLA4B. The green line shows the residuals obtained subtracting the formamide emission from the $CH_3OCH_3$ profile. The two vertical dashed lines show the position of VLA4A (black) and VLA4B (red). The offset in pixel is given with respect to the position of VLA4A. The pixel size corresponds to 25 mas. Right panel: residual line profiles of $CH_3OCH_3$ (green), $CH_3OH$ (orange), $^{13}CH_3OH$ (blue), and $CH_3CHO$ (magenta), after subtracting the formamide emission profile. The analyzed lines are the $CH_3OCH_3$ line at 241.964 GHz, the $CH_3OH$ line at 241.904 GHz, the $^{13}CH_3OH$ line at 255.204 GHz, the two detected $CH_3CHO$ lines at 242.106 GHz and 242.118 GHz, whose intensity is added, and the $NH_2CHO$ line at 243.521 GHz.

investigate the species spatial distribution, we compare emission lines with similar $E_{up}$ (between 57 and 81 K) in order to minimize excitation conditions effects. Figure 3 shows the normalized integrated line profiles of $CH_3OCH_3$ and $NH_2CHO$, extracted along the horizontal axes connecting the two protostars (Figure 2). The $x$-axis reports the offset in astronomical units with respect to the position of VLA4A. Two vertical dashed lines indicate the positions of the two protostars. The green line is the residual emission obtained subtracting the $NH_2CHO$ spectra from the $CH_3OCH_3$ emission. If we assume that $NH_2CHO$ mainly traces VLA4A, the green profile is the additional emission from VLA4B. Figure 3 also shows the residual profiles of $CH_3OCH_3$, $CH_3OH$, $^{13}CH_3OH$, and $CH_3CHO$ after subtracting the $NH_2CHO$ emission. The figure highlights the emission of different species at the position of VLA4B. Finally, Figure A1 shows the intensity-weighted peak velocity (moment 1) maps of the brightest $^{13}CH_3OH$, $CH_3OCHO$, and $NH_2CHO$ lines. All of the lines show velocity gradients roughly orthogonal to the outflow direction. Methanol shows the broadest velocity interval while formamide shows the tightest.

### 3.3. Column Densities and Abundances

In order to characterize the two hot corinos, we analyzed their methanol emission on the dust peaks (Table 1) via the non-LTE LVG (large velocity gradient) code `grelvg`, developed by Ceccarelli et al. (2003). We used the collisional coefficients with para-$H_2$, computed by Rabli & Flower (2010) between 10 and 200 K for the first 256 levels and provided by the BASECOL database (Dubernet et al. 2013). We assumed the A/E $CH_3OH$ ratio equal to 1 (Flower et al. 2006) and $^{12}C/^{13}C = 60$ (e.g., Milam et al. 2005). To compute the line escape probability as a function of the line optical depth, we adopted a semi-infinite slab geometry and a line width equal to 4 km s$^{-1}$, as measured. We ran a large grid of models (~10,000) to cover the $\chi^2$ surface in the parameters space: the total (A- plus E- ) methanol column density N($CH_3OH$) from $1 \times 10^{13}$ to $2 \times 10^{18}$ cm$^{-2}$, the $H_2$ density $n_{H2}$ from $1 \times 10^5$ to $\times 10^{10}$ cm$^{-3}$ and the temperature T from 40 to 200 K. We fitted the measured $^{13}CH_3OH$-A line intensities by comparing them with those predicted by the model, leaving $N(^{13}CH_3OH)$, $n_{H2}$, and $T$ as free parameters. We obtained a good fit ($\chi^2 = 1.1$) with the following parameters: $N(^{13}CH_3OH) = (1.0 \pm 0.2) \times 10^{17}$ cm$^{-2}$, $T = (140 \pm 40)$ K, and $n_{H2} = 3 \times 10^8$ cm$^{-3}$ with a lower limit of $2 \times 10^7$ cm$^{-3}$, indicating that the lines are LTE populated.[6] Line optical depths are estimated using the non-LTE predictions. The predicted opacity of the $^{13}CH_3OH$-A line is between 0.1 to 0.4. Because the $^{12}CH_3OH$-E lines are predicted to be very optically thick ($\tau \sim 60$), we derive the column density of the main isotopologue from the $^{13}CH_3OH$ one, assuming the same temperature of 140 K, and we obtain $N(CH_3OH) = (6 \pm 1) \times 10^{18}$ cm$^{-2}$. We repeated the same analysis also for VLA4B and obtained the following parameters (reduced $\chi^2 = 0.95$): $N(CH_3OH) = (5 \pm 1) \times 10^{18}$ cm$^{-2}$, $T = (170 \pm 50)$ K, and $n_{H2} = 3 \times 10^8$ cm$^{-3}$ with a lower limit of $2 \times 10^7$ cm$^{-3}$, again indicating that the lines are LTE populated. Please note that the line with $E_{up} = 800$ K cannot be modeled by the non-LTE code because of the lack of collisional coefficients. Assuming that the line upper level is LTE populated, the predicted intensity is

[6] Note that the obtained values are in good agreement with those derived by the non-LTE analysis of 18 $^{13}CH_3OH$ lines detected by the IRAM 30 m ASAI survey (Bianchi et al. 2017).

**Table 2**
Results of the Non-LTE LVG and LTE Rotational Diagram Analysis of the iCOM Emission Observed toward VLA4A and VLA4B

| Species | VLA4A | | | VLA4B | | | VLA4A/VLA4B[a] |
|---|---|---|---|---|---|---|---|
| | $T_{rot}$ (K) | $N_{tot}$ ($cm^{-2}$) | $X_{CH_3OH}$[b] | $T_{rot}$ (K) | $N_{tot}$ ($cm^{-2}$) | $X_{CH_3OH}$[c] | |
| Non-LTE Analysis | | | | | | | |
| $CH_3OH$[c] | 140[d] | $6(1) \times 10^{18}$ | … | 170[d] | $5(1) \times 10^{18}$ | … | 1.2 (0.3) |
| $^{13}CH_3OH$ | 140(40) | $1.0(0.2) \times 10^{17}$ | … | 170(50) | $8(2) \times 10^{16}$ | … | 1.3 (0.4) |
| Rotational Diagram Analysis | | | | | | | |
| $CH_3CHO$ | 140[d] | $2.4(0.4) \times 10^{16}$ | $4.0\ (1.0) \times 10^{-3}$ | 170[d] | $1.1(0.2) \times 10^{16}$ | $2.2\ (0.6) \times 10^{-3}$ | 2.2 (0.5) |
| $CH_3OCH_3$ | 140[d] | $7.5(1.2) \times 10^{16}$ | $1.3\ (0.3) \times 10^{-2}$ | 170[d] | $1.0(0.2) \times 10^{17}$ | $2.0\ (0.6) \times 10^{-3}$ | 0.8 (0.2) |
| $NH_2CHO$ | 140[d] | $5.9(0.9) \times 10^{15}$ | $4.0\ (0.9) \times 10^{-3}$ | 170[d] | $1.4(0.3) \times 10^{15}$ | $2.8\ (0.8) \times 10^{-4}$ | 4 (1) |

**Notes.**
[a] Column density ratios.
[b] Abundance ratio with respect to $CH_3OH$.
[c] Derived from $^{13}CH_3OH$ assuming $^{12}C/^{13}C = 60$.
[d] Assumed, as derived by the methanol non-LTE analysis.

about a factor of 2 lower than the observed one.[7] Yet, it is very likely this high-lying line is subthermally populated so that the predicted intensity even has to be considered an upper limit. It has already been found by other authors that high-lying (with $E_{up} \geqslant 500$ K) methanol lines are most likely due to radiatively populated methanol rather than collisionally populated, as discussed in Leurini et al. (2007).

Because the methanol non-LTE analysis showed that both the VLA4A and VLA4B hot corinos have large densities, we carried out an LTE rotational diagram analysis for the other iCOMs, assuming a rotational temperature of 140 and 170 K for VLA4A and VLA4B, respectively, as derived from the methanol analysis. The results of the analysis are reported in Table 2. Synthetic LTE spectra generated using Weeds (Maret et al. 2011) are reported in Figures E1–E4. The column density ratios between VLA4A and VLA4B are consistent with the line intensity ratios reported in Table 1. In Table 2 we also report the column density ratios of the other iCOMs with respect to methanol, which is in agreement with the ASAI analysis (Bianchi et al. 2019).

## 4. Discussion and Conclusions

### 4.1. Accretion Streamers and Hot Corinos

The three continuum arc structures observed toward the south and the three fingers toward the north could be either accretion streamers or alternatively, outflow cavity walls. The brightest arc-like structure in the south has been reported on similar spatial scales by Tobin et al. (2018) in the 1.3 mm continuum emission and in blueshifted $C^{18}O$(2–1) emission. Tobin et al. (2018) stressed that this one-armed spiral pattern is similar to that observed in L1448 IRAS3B (Tobin et al. 2016) and associated with a disk inclined by ∼45° surrounding the triple system. The SVS13-A disks are closer to edge on (i = 67° and 50°) than L1448 IRAS3B. Although the contribution of cavities opened by the precessing jets/outflows cannot be excluded, recent studies have shown that accretion streamers feeding disks are common phenomena from Class 0 to Class II objects (Yen et al. 2019; Pineda et al. 2020; Garufi et al. 2022), where planet formation is possibly already ongoing. Their presence may strongly affect the disk chemical composition because they can produce slow shocks when impacting the disk. The chemistry occurring in the shocked gas could synthesize new molecules that would eventually accrete into the disk and, consequently, enrich it. Further observations of typical shock tracers such as SO and $SO_2$ (e.g., Garufi et al. 2022) are needed to confirm the presence of accretion streamers in VLA4A and VLA4B.

On the other hand, iCOM emission is compact, confirming the presence of two hot corinos, one in VLA4A and a second one in VLA4B. The molecular emission sizes (0.″3–0.″5) are consistent with thermal sublimation of the icy mantles, namely the classical definition of a hot corino (Ceccarelli 2004). The velocity gradient roughly perpendicular to the outflow direction (see Figure A1) suggests the presence of rotating gas, either from two protostellar disks or from the inner portion of the infalling envelope.

Thanks to the superb angular resolution (0.″13 in the east–west direction), the blueshifted line emission appears to be elongated in the north direction up to ∼150 au, being spatially coincident with the northern accretion streamers (Figure C1–C5). The iCOM emission could be associated with material accreting from the streamer and inducing a slow shock in the protostellar disk, similarly to what was found in, e.g., L1527 (Sakai et al. 2014; Oya et al. 2015; Sakai et al. 2017). Moreover, we cannot exclude the possibility that the system has a higher multiplicity, including multiple unresolved cores. Observations of different molecular tracers at extremely high angular resolution (tens of astronomical units), as well as an accurate physical model of the system, are necessary to conclude the origin of iCOM emission.

Finally, the data suggest chemical segregation between formamide, tracing mainly VLA4A and the rest of the observed iCOMs, in the inner 100 au of the system. In Appendix D we discuss the possibility that the observed chemical segregation is due to opacity effects. While dust and line opacity effects cannot completely be excluded, our data suggest a real chemical differentiation of the two hot corinos instead of temperature gradients or excitation effects.

[7] Note that we used the same beta escape probability $\beta$ as a function of the line opacity $\tau$ used in the non-LTE LVG code, namely $\beta = \frac{1-\exp[-3\tau]}{3\tau}$(de Jong et al. 1980), where $\tau$ is estimated to be 0.3.

### 4.2. A Real Chemical Segregation?

A different spatial distribution between O-bearing and N-bearing molecules has been observed in Orion KL (Blake et al. 1987; Peng et al. 2013, and references therein) and in other high-mass star-forming regions on scales of thousands of astronomical units (Allen et al. 2017; Csengeri et al. 2019). Investigating whether a similar segregation is present also in the inner 100 au around low-mass protostars is more complicated as only a few system have been observed with enough angular resolution. An intriguing chemical segregation between formamide and acetaldehyde has been observed in the jet-induced shock L1157-B1, at a distance of >0.1 pc from the protostar (Codella et al. 2017). In this case, the dichotomy is reproduced well by chemical models that assume that the formamide formation is dominated by gas-phase reactions (chemistry effect). A chemical differentiation has also been observed in the prototypical Class 0 binary system IRAS 16293–2422 (Manigand et al. 2020). The abundance of $CH_3OCH_3$ relative to methanol is similar in the two components of the IRAS 16293–2422 system, while it differs by a factor of 2 for $CH_3CHO$ and 4 for $NH_2CHO$, similarly to what was found in VLA4A and VLA4B. In IRAS 16293–2422, the observed differences are interpreted as a result of the onion-like structure of the hot corino (physical effect). In particular, the $NH_2CHO$ rotational temperature is slightly higher ($T \sim 140$–$300$ K) than what was derived for other iCOMs ($T \sim 100$ K) (Jørgensen et al. 2016, 2018; Manigand et al. 2020), suggesting that N-bearing species trace hotter gas, closer to the protostar. On the other hand, recent ALMA observations of other two Class 0 protostars, Perseus B1-c and Serpens S68N, do not show a significant difference in the excitations conditions of N-bearing and O-bearing species (van Gelder et al. 2020; Nazari et al. 2021), leaving the question open. Further observations in different N-bearing and O-bearing complex species are required to clarify the origin of the chemical segregation observed in SVS13-A and inferred in IRAS 16293–2422 A and B but not in other low-mass protostars. The spatial distribution of iCOM emission in SVS13-A supports the idea that formamide is formed in a compact region closer to the protostar and thus, contrarily to other iCOMs, can be more easily obscured by the dust. The fact that the dust emission of VLA4B is optically thicker than that of VLA4A supports this scenario. Note also that the binding energy, recently computed by Ferrero et al. (2020), of formamide (average ∼8400 K) is larger than the one of methanol (average ∼6200 K), in agreement with the possible onion-like structure of the two SVS13-A hot corinos. Interestingly, Diaz-Rodriguez et al. (2021) report the detection of ethylene glycol only toward VLA4A, suggesting that the observed chemical segregation in SVS13-A is not exclusive of formamide. Because no binding energy of ethylene glycol is available in the literature, we carried out new ab initio quantum chemistry calculations to evaluate its binding energy over an 18 water molecule cluster (see Appendix F). In order to compare ethylene glycol with formamide, we also recalculated the binding energy of the latter. We found that the binding energy of ethylene glycol has an average value of ∼7100 K, while that of formamide is equal to ∼4700 K. We emphasize that the difference with respect to Ferrero et al. (2020) is due to a different water cluster used. The important point here is the relative binding energy of ethylene glycol with respect to formamide, which is not expected to change with the water cluster used. This means that if the calculation by Ferrero et al. (2020) was performed for ethylene glycol, the binding energy would be even higher than that of formamide (∼8400 K). This justifies the similar spatial distribution of formamide and ethylene glycol, different from that of methanol. Overall, the new calculated binding energies support the hypothesis that the observed chemical differentiation is caused by the onion-like structure of the two SVS13-A hot corinos instead of spatial segregation between O-bearing and N-bearing species. Further observations at high angular resolution (tens of astronomical units) with ALMA and at centimeter wavelengths with JVLA (and, in the future, with ngVLA and SKA) are needed to further investigate the chemical stratification inside the two hot corinos VLA4A and VLA4B and to quantify the dust opacity effects.

The authors thank the anonymous referee for the constructive comments, which substantially helped improve the quality of the paper. This project has received funding from (1) the European Research Council (ERC) under the European Union's Horizon 2020 research and innovation program, for the Project The Dawn of Organic Chemistry (DOC), grant agreement No 741002; (2) the PRIN-INAF 2016 The Cradle of Life—GENESIS-SKA (General Conditions in Early Planetary Systems for the rise of life with SKA); (3) the European Unions Horizon 2020 research and innovation programs under projects Astro-Chemistry Origins (ACO), Grant No 811312. This paper makes use of the following ALMA data: ADS/JAO.ALMA#2018.1.01461.S. ALMA is a partnership of ESO (representing its member states), NSF (USA) and NINS (Japan), together with NRC (Canada), MOST and ASIAA (Taiwan), and KASI (Republic of Korea), in cooperation with the Republic of Chile. The Joint ALMA Observatory is operated by ESO, AUI/NRAO and NAOJ. Most of the computations presented in this paper were performed using the GRICAD infrastructure (https://gricad.univ-grenoble-alpes.fr), which is partly supported by the Equip@Meso project (reference ANR-10-EQPX-29-01) of the program Investissements d'Avenir supervised by the Agence Nationale pour la Recherche. Additionally this work was granted access to the HPC resources of IDRIS underthe allocation 2019-A0060810797 attributed by GENCI (GrandEquipement National de Calcul Intensif).

*Software:* astropy (Astropy Collaboration et al. 2013, 2018), matplotlib (Hunter 2007), GAUSSIAN16 (Frisch et al. 2016), CASA (McMullin et al. 2007).

## Appendix A
## Moment 1 Maps

Figure A1 reports the intensity-weighted velocity peak (moment 1) maps of the following lines: $^{13}CH_3OH$ at 256.8265 GHz, $CH_3CHO$ at 242.1060 GHz, and $NH_2CHO$ at 255.058 GHz. The two stars indicate the VLA4A and VLA4B positions. The systemic velocities of the two protostars are indicated as horizontal lines in the wedge.

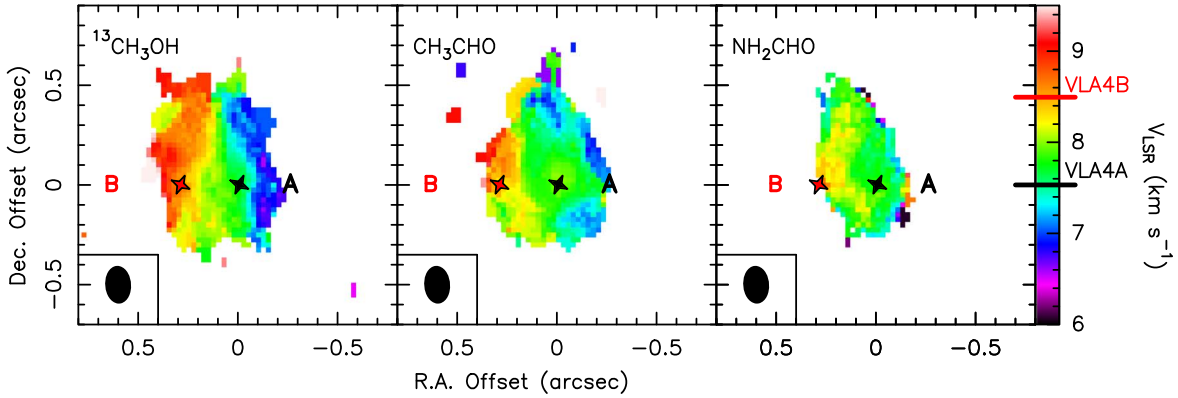


**Figure A1.** Moment 1 (intensity-weighted velocity peak) map of the lines $^{13}CH_3OH$ at 256.8265 GHz, $CH_3CHO$ at 242.1060 GHz, and $NH_2CHO$ at 255.058 GHz (see Table 1). The two stars indicate the VLA4A and VLA4B positions. The systemic velocities of the two protostars are indicated as horizontal lines in the wedge.

## Appendix B
## ALMA Observations

Table B1 reports the parameters of the observed ALMA setup.

**Table B1**
Observations

| Frequencies (GHz) | Synthesized beam (″) | rms (mJy/beam kms$^{-1}$ ) | Detected Transitions |
|---|---|---|---|
| 241.528–241.647 | 0.″21 × 0.″14 | 4.8 | $CH_3OH$ $25_{3,22}$–$25_{2,23}$ A<br>$CH_3OCH_3$ $5_{3,2}$–$4_{2,3}$ EA, AE, EE, AA<br>$CH_3OCH_3$ $21_{3,18}$–$20_{4,17}$ EA, AE, EE, AA |
| 241.900–242.020 | 0.″21 × 0.″14 | 4.9 | $CH_3OH$ $5_{2,3}$–$4_{2,2}$ E<br>$CH_3OH$ $5_{-2,4}$–$4_{-2,3}$ E<br>$CH_3OCH_3$ $13_{1,13}$–$12_{0,12}$ EA, AE, EE, AA |
| 242.076–242.135 | 0.″20 × 0.″13 | 4.8 | $CH_3CHO$ $13_{1,13}$–$12_{1,12}$ E, A |
| 243.491–243.550 | 0.″22 × 0.″14 | 6.2 | $NH_2CHO$ $12_{1,12}$–$11_{1,11}$ |
| 255.020–255.080 | 0.″20 × 0.″13 | 5.3 | $NH_2CHO$ $12_{4,9}$–$11_{4,8}$<br>$NH_2CHO$ $12_{4,8}$–$11_{4,7}$ |
| 255.196–255.255 | 0.″20 × 0.″13 | 5.3 | $CH_3OH$ $16_{3,14}$–$16_{2,15}$ A<br>$^{13}CH_3OH$ $4_{3,2}$–$4_{2,3}$ A<br>$^{13}CH_3OH$ $3_{3,0}$–$3_{2,1}$ A<br>$^{13}CH_3OH$ $7_{3,5}$–$7_{2,6}$ A<br>$^{13}CH_3OH$ $3_{3,1}$–$3_{2,2}$ A |
| 256.107–256.167 | 0.″19 × 0.″13 | 5.1 | $CH_3OCH_3$ $19_{5,14}$–$19_{4,15}$ AE, EA, EE, AA |
| 256.797–256.856 | 0.″19 × 0.″13 | 5.6 | $^{13}CH_3OH$ $14_{3,12}$–$14_{2,13}$ A<br>$CH_3OCH_3$ $19_{5,14}$–$19_{4,15}$ AE, EA, EE, AA |

## Appendix C
## Channel Maps of the Present ALMA Data Set

In this section, we report the images of all the 17 transitions of the 4 iCOMs ($CH_3OH$, $^{13}CH_3OH$, $CH_3CHO$, $NH_2CHO$, and $CH_3OCH_3$) observed in SVS13-A.

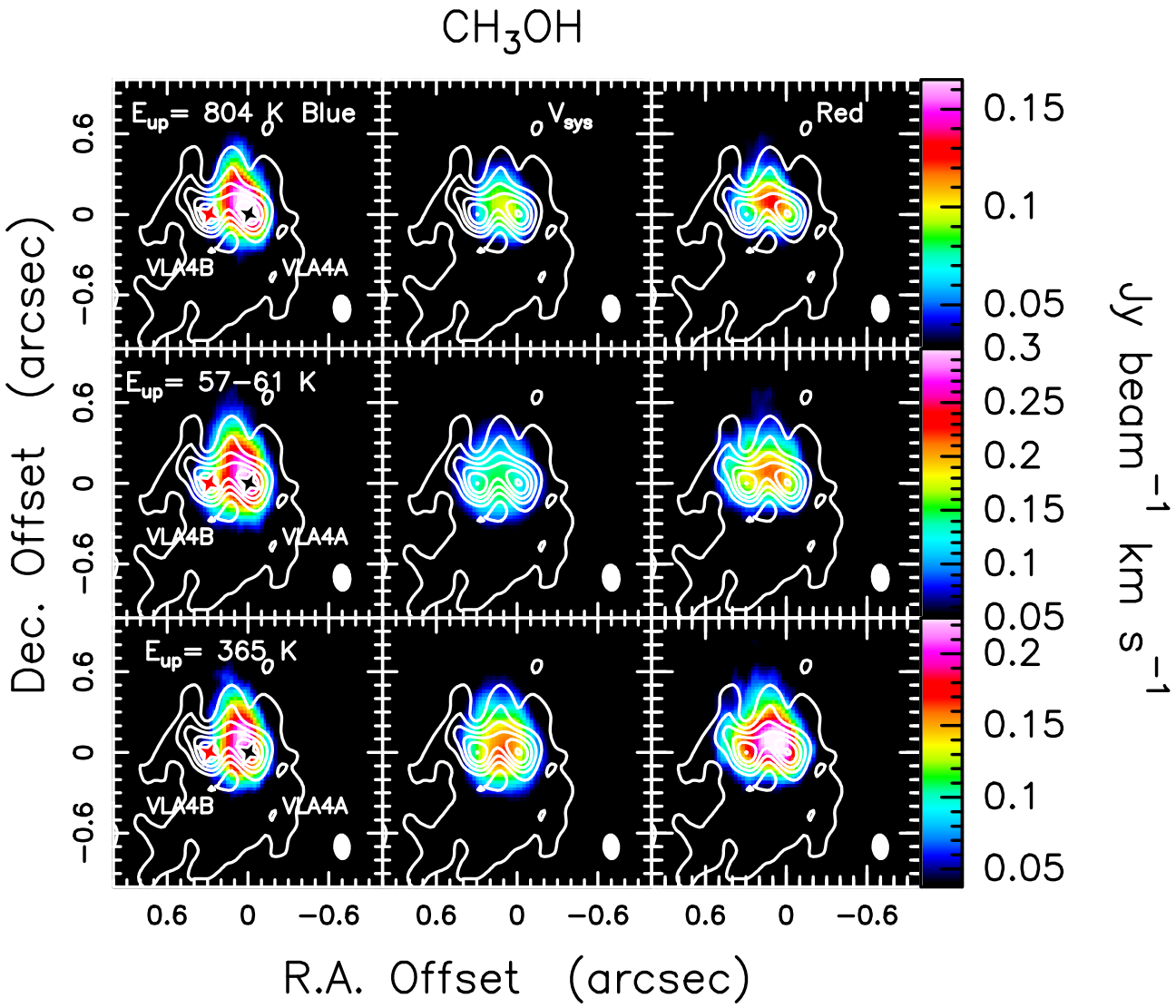


**Figure C1.** Integrated emission of all the detected lines of $CH_3OH$, in color scale, superposed on the dust emission in white contours. The emission is integrated in the following velocity intervals: 4–7.5 km s$^{-1}$ in the left panels (blue), 7.5–8.7 km s$^{-1}$ in the middle panels ($V_{sys}$), and 8.8–12.0 km s$^{-1}$ in the right panels (red). The first contours are 10$\sigma$, corresponding to 4 mJy beam$^{-1}$, and steps are 25$\sigma$, corresponding to 10.46 mJy beam$^{-1}$. The synthesized beams are reported in white in the lower-right corner of each panel. On the left is reported the upper-level energy of each transition in Kelvin.

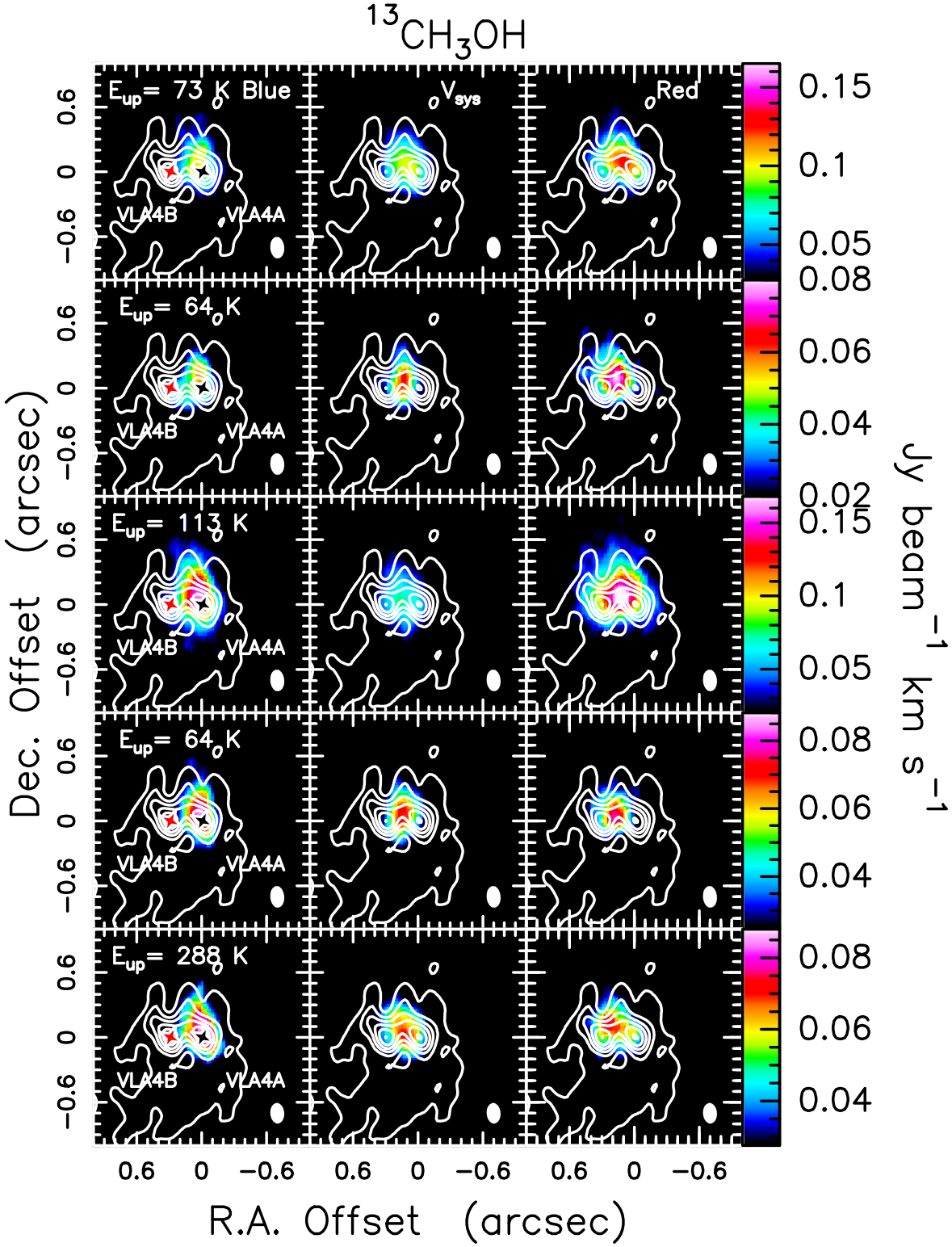


**Figure C2.** Integrated emission of all the detected lines of $^{13}CH_3OH$, in color scale, superposed on the dust emission in white contours. The emission is integrated in the following velocity intervals: 4–7.5 km s$^{-1}$ in the left panels (blue), 7.5–8.7 km s$^{-1}$ in the middle panels ($V_{sys}$), and 8.8–12.0 km s$^{-1}$ in the right panels (red). The first contours are 10$\sigma$, corresponding to 4 mJy beam$^{-1}$, and steps are 25$\sigma$, corresponding to 10.46 mJy beam$^{-1}$. The synthesized beams are reported in white in the lower-right corner of each panel. On the left is reported the upper-level energy of each transition in Kelvin.

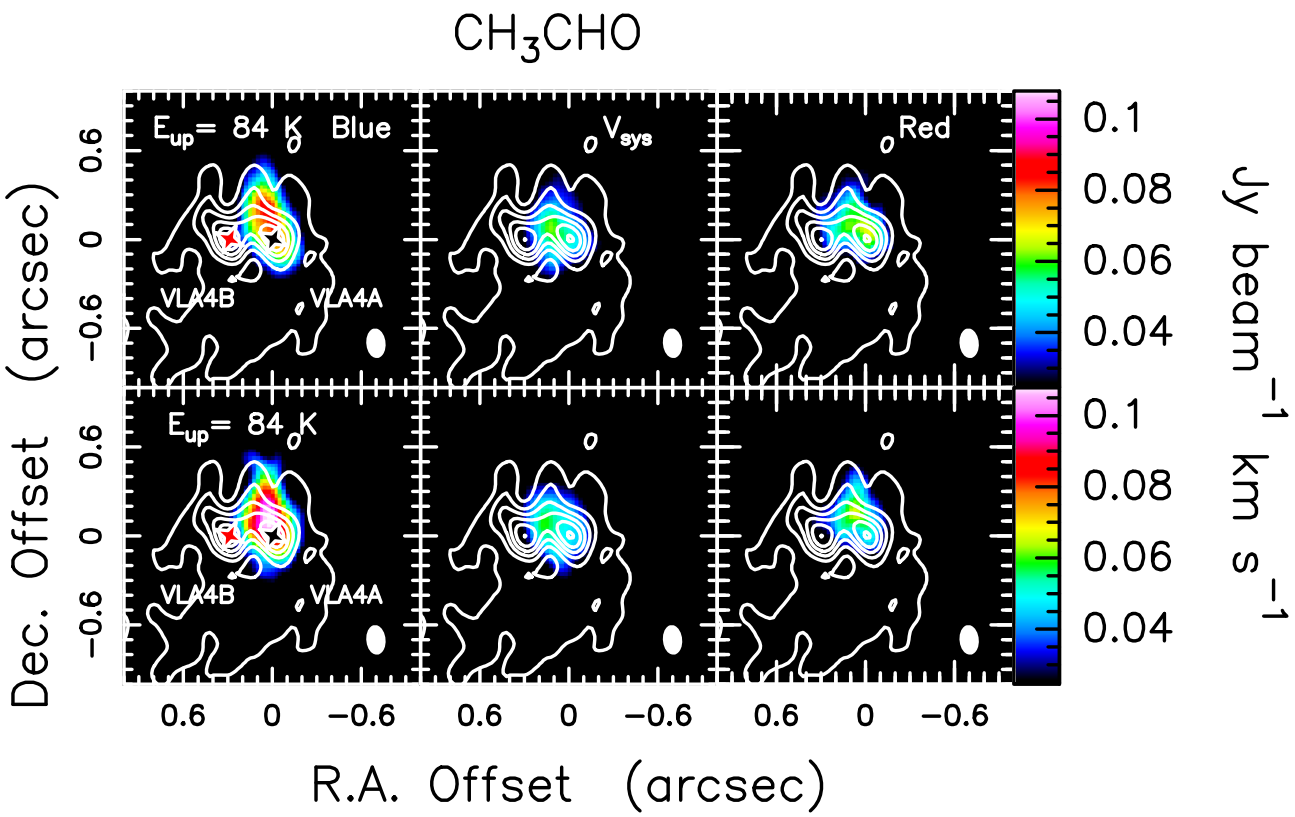


**Figure C3.** Integrated emission of all the detected lines of $CH_3CHO$, in color scale, superposed on the dust emission in white contours. The emission is integrated in the following velocity intervals: 4–7.5 km s$^{-1}$ in the left panels (blue), 7.5–8.7 km s$^{-1}$ in the middle panels ($V_{sys}$), and 8.8–12.0 km s$^{-1}$ in the right panels (red). The first contours are 10$\sigma$, corresponding to 4 mJy beam$^{-1}$, and steps are 25$\sigma$, corresponding to 10.46 mJy beam$^{-1}$. The synthesized beams are reported in white in the lower-right corner of each panel. On the left is reported the upper-level energy of each transition in Kelvin.

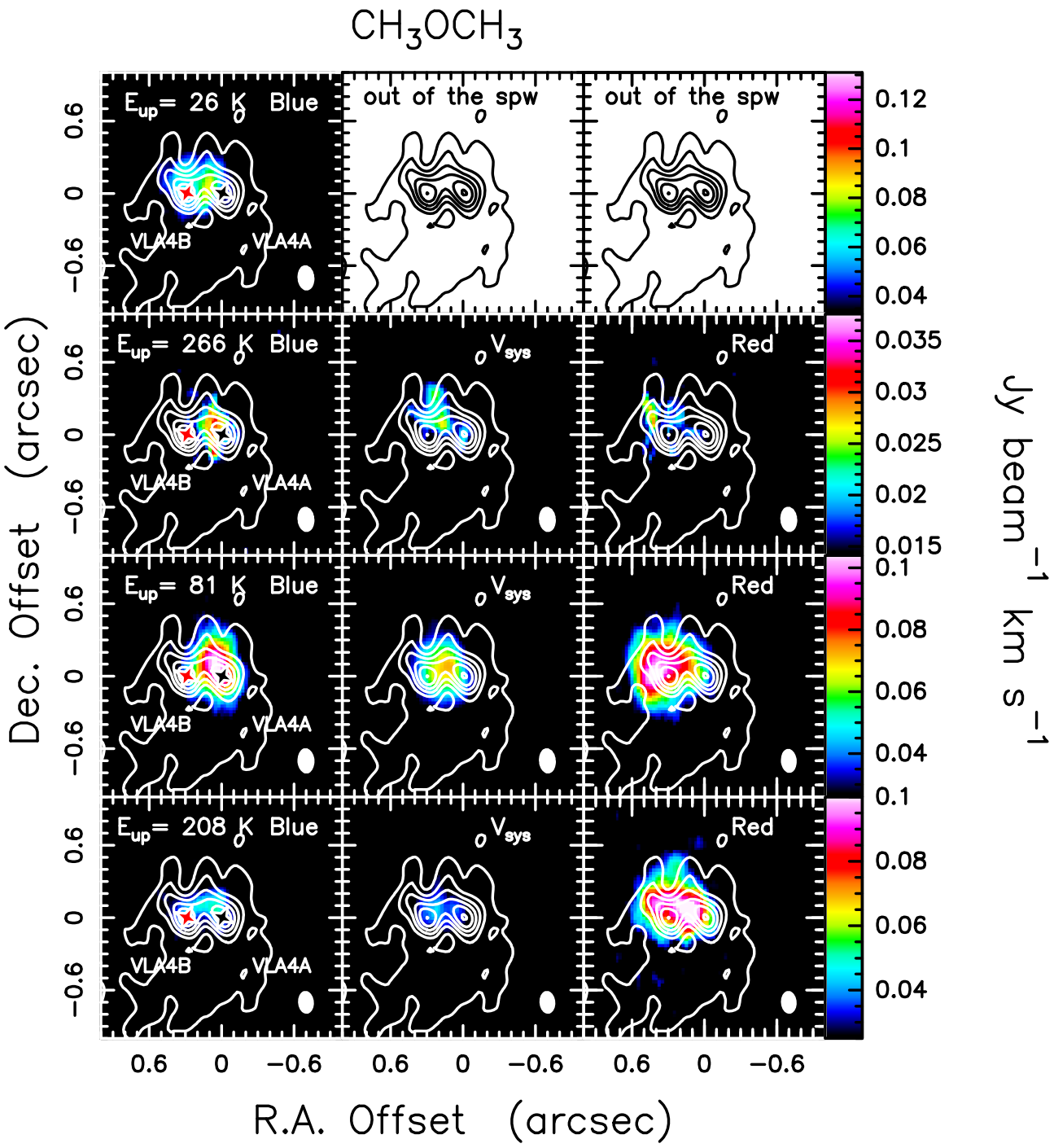


**Figure C4.** Integrated emission of all the detected lines of $CH_3OCH_3$, in color scale, superposed on the dust emission in white contours. The emission is integrated in the following velocity intervals: 4–7.5 km s$^{-1}$ in the left panels (blue), 7.5–8.7 km s$^{-1}$ in the middle panels ($V_{sys}$), and 8.8–12.0 km s$^{-1}$ in the right panels (red). The first contours are 10$\sigma$, corresponding to 4 mJy beam$^{-1}$, and steps are 25$\sigma$, corresponding to 10.46 mJy beam$^{-1}$. The synthesized beams are reported in white in the lower-right corner of each panel. On the left is reported the upper-level energy of each transition in Kelvin. The panels showing only the continuum contours refer to line emission partially outside the observed spectral window (spw). Please note that each line is composed of four blended transitions very close in frequency (AE, EA, EE, AE). This structure, due to the rotation in the $CH_3OCH_3$ molecule of two functional groups $CH_3$-, leads to some contamination in the channel maps. However, we would like to stress that this velocity blending does not affect the line spatial distribution.

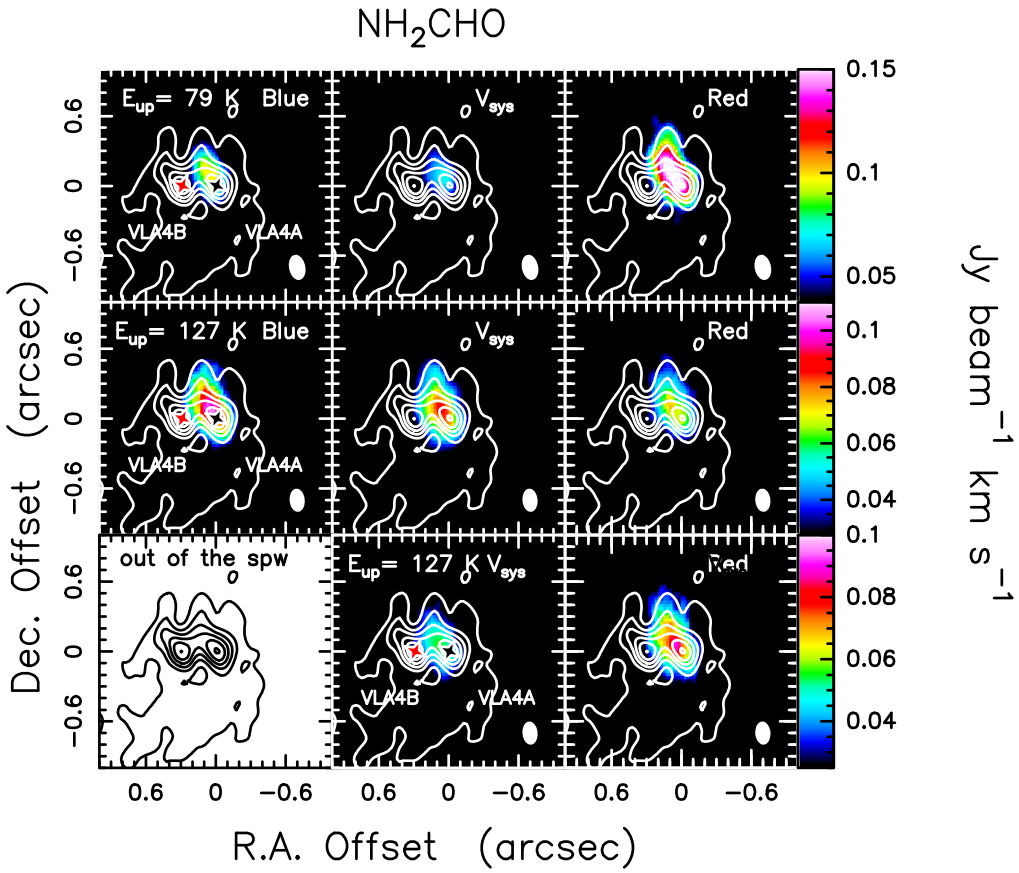


**Figure C5.** Integrated emission of all the detected lines of $NH_2CHO$, in color scale, superposed on the dust emission in white contours. The emission is integrated in the following velocity intervals: 4–7.5 km s$^{-1}$ in the left panels (Blue), 7.5–8.7 km s$^{-1}$ in the middle panels ($V_{sys}$), and 8.8–12.0 km s$^{-1}$ in the right panels (Red). The first contours are 10$\sigma$, corresponding to 4 mJy beam$^{-1}$, and steps are 25$\sigma$, corresponding to 10.46 mJy beam$^{-1}$. The synthesized beams are reported in white in the lower-right corner of each panel. On the left is reported the upper-level energy of each transition in Kelvin. The panel showing only the continuum contours refers to line emission partially outside the observed spectral window (spw).

## Appendix D
## Dust and Line Opacity Effects

Previous studies of the binary system IRAS 4A have shown that dust could dramatically obscure molecular emission at (sub)millimeter wavelengths (De Simone et al. 2020). In particular, while iCOM emission is observed only toward one of the two protostars of the binary system at (sub)millimeter wavelengths (López-Sepulcre et al. 2017), a similar emission is instead observed at radio wavelengths, which are less affected by dust opacity (De Simone et al. 2020). In the case of the binary system SVS13-A, dust opacity effects may also play a role. In particular, at 1.2 mm, the flux density of VLA4A is higher by a factor of 1.4 with respect to that of VLA4B, while VLA4B is brighter at shorter wavelengths (Diaz-Rodriguez et al. 2021). Moreover, the spectral index is different toward the two sources (2.2–2.4 in VLA4B and 3.0–3.1 in VLA4A). This suggests (a) possible grain growth toward VLA4B, implying a large fraction of large dust grains that enhance the flux at 9 mm wavelengths or, alternatively, (b) optically thick dust at 1.3mm toward VLA4B. In this second hypothesis, dust opacity could prevent us from detecting molecular emission toward VLA4B, similarly to the case of IRAS 4A. In any case, as all the observed transitions are at similar frequencies, dust opacity is expected to affect the emission from iCOMs in the same way if they originate from the same region. Another explanation for a different spatial distribution of molecular species could be line opacity. Optically thick lines could trace an external shell of the protostellar envelope, more extended than the one traced by optically thin lines. The simultaneous observations of lines covering a broad range of upper-level energies (26–804 K) allow us to verify that molecular lines from the same species show a similar spatial distribution, regardless of the upper-level energy of the transition (see Figures C1–C5). We conclude that the observed iCOM spatial distribution is not driven by excitation effects.

## Appendix E
## Comparison with LTE Modeling

We report here the synthetic LTE spectra generated with Weeds using the gas parameter derived from the LVG and rotational diagram analysis (see Section 3.3).

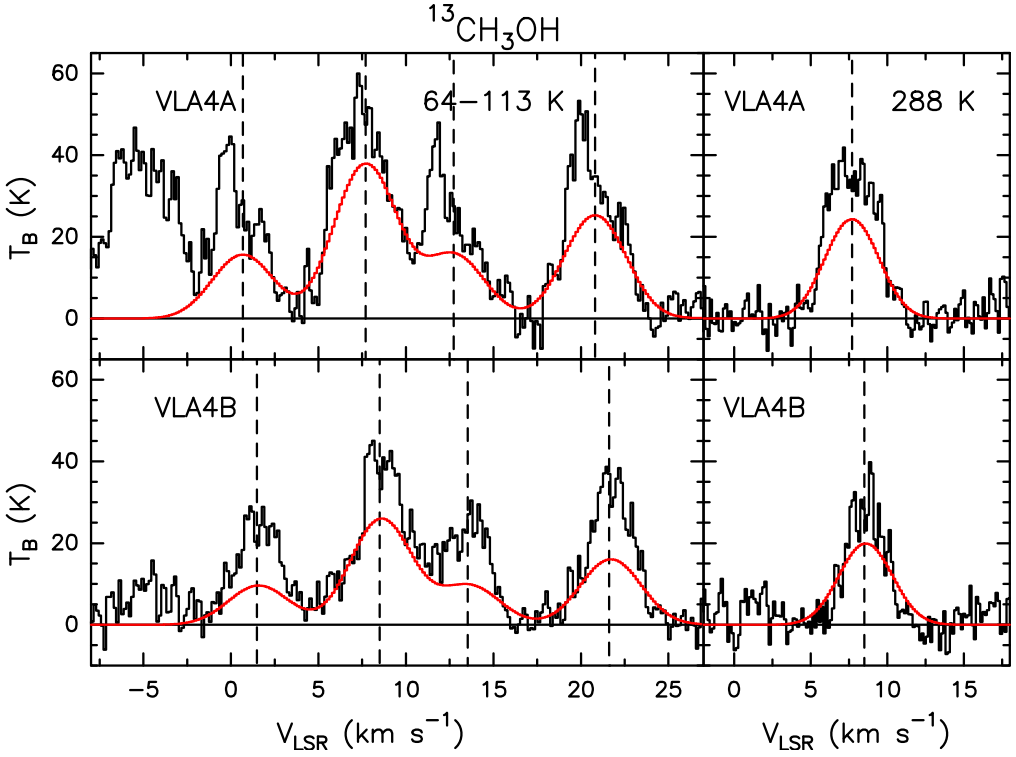


**Figure E1.** Synthetic LTE spectra generated with Weeds using the gas parameter in Table 2.

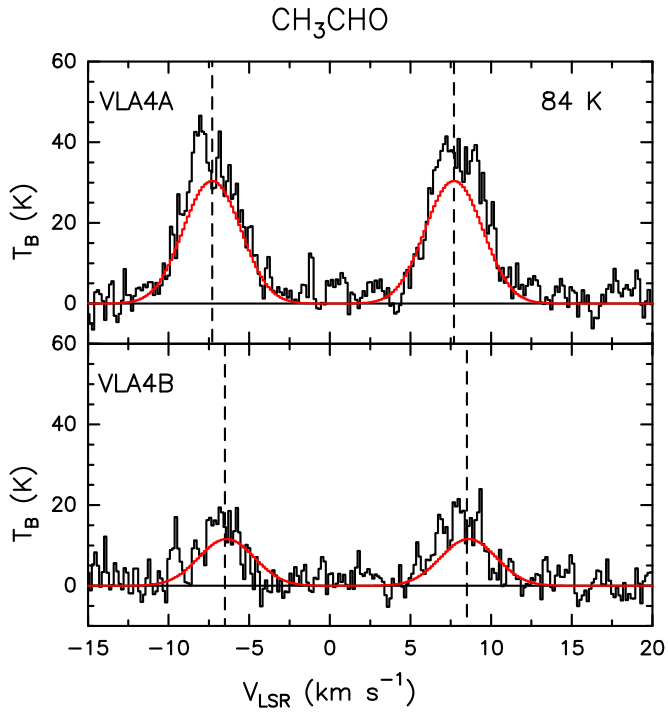


**Figure E2.** Synthetic LTE spectra generated with Weeds using the gas parameter in Table 2.

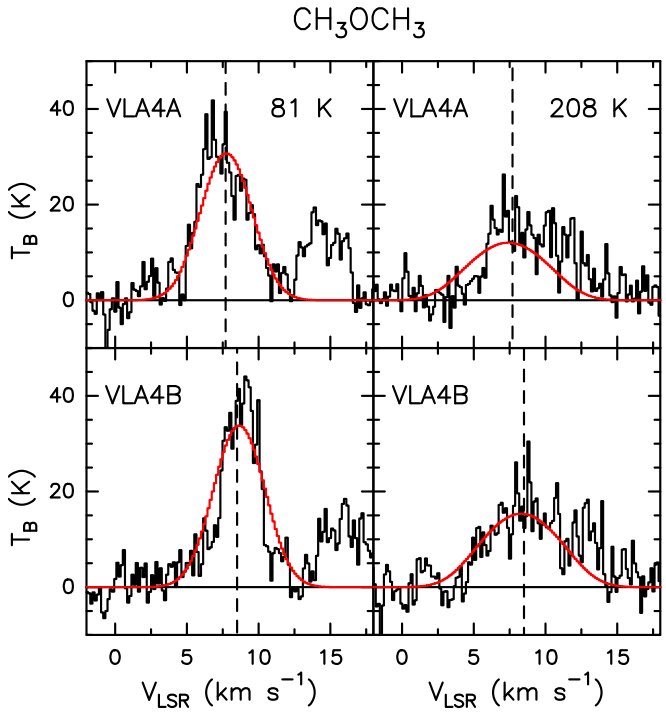


**Figure E3.** Synthetic LTE spectra generated with Weeds using the gas parameter in Table 2.

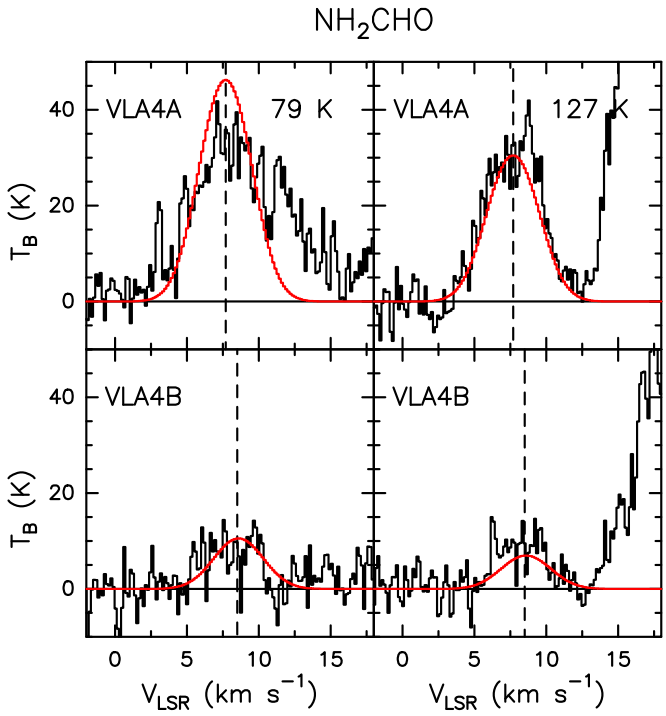


**Figure E4.** Synthetic LTE spectra generated with Weeds using the gas parameter in Table 2.

## Appendix F
## Quantum Chemical Computations

We have carried out quantum chemical calculations with the GAUSSIAN16 (Frisch et al. 2016) in order to calculate the binding energies of ethylene glycol and formamide on an amorphous water-ice surface made of 18 water molecules. We employed the hybrid-DFT functional BHandHLYP (Lee et al. 1988; Becke 1993), corrected for dispersion with Grimme's G3(BJ) a posteriori correction (Grimme et al. 2010, 2011). Geometry optimization and frequency calculations were carried out with the 6-311+G(d,p) basis set (Hehre et al. 1972; Hariharan & Pople 1973; Krishnan et al. 1980). Density functional theory (DFT) energies were further refined at the 6-311++G(2df,2pd). This functional has been shown to provide high-quality binding energies for organic fragments (e.g., Enrique-Romero et al. 2019, 2021, 2022).

Several binding geometries were found for each molecule. For each one of them, we provide a binding energy value calculated following $E_{\rm bind} = -(E_{\rm complex} - E_{\rm admol} - E_{\rm surf})$, where $E_{\rm complex}$, $E_{\rm admol}$, and $E_{\rm surf}$ correspond to the zero-point-corrected energies of the complex (surface + molecule), the molecule (isolated), and the surface (isolated), respectively. Both the geometries and their binding energy values are shown Figure F1.

As can be seen, ethylene glycol has a higher binding energy, ranging from ∼50–70 kJ mol$^{-1}$ (6300–8400 K), than formamide (∼25–55 kJ mol$^{-1}$, 2970–6600K) as a consequence of its flexibility and size, which allow ethylene glycol to establish two to four H bonds, while formamide can only make two to three at most, on our water surface model.

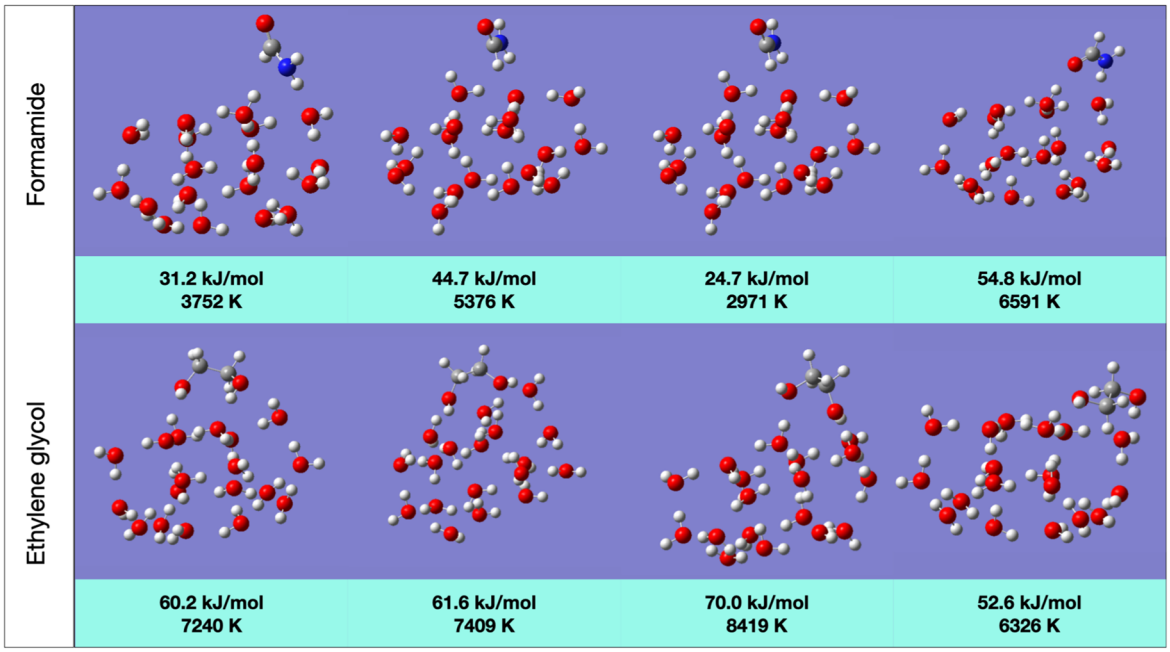


**Figure F1.** Optimized binding geometries and energies. The energetics include zero-point-energy corrections.

## ORCID iDs

Eleonora Bianchi https://orcid.org/0000-0001-9249-7082
Ana López-Sepulcre https://orcid.org/0000-0002-6729-3640
Cecilia Ceccarelli https://orcid.org/0000-0001-9664-6292
Claudio Codella https://orcid.org/0000-0003-1514-3074
Linda Podio https://orcid.org/0000-0003-2733-5372
Mathilde Bouvier https://orcid.org/0000-0003-0167-0746
Joan Enrique-Romero https://orcid.org/0000-0002-2147-7735

## References

Allen, V., van der Tak, F. F. S., Sánchez-Monge, Á, Cesaroni, R., & Beltrán, M. T. 2017, A&A, 603, A133
Astropy Collaboration, Robitaille, T. P., Tollerud, E. J., et al. 2013, A&A, 558, A33
Astropy Collaboration, Price-Whelan, A. M., Sipőcz, B. M., et al. 2018, AJ, 156, 123
Becke, A. D. 1993, JChPh, 98, 1372
Belloche, A., Maury, A. J., Maret, S., et al. 2020, A&A, 635, A198
Bianchi, E., Codella, C., Ceccarelli, C., et al. 2017, MNRAS, 467, 3011
Bianchi, E., Codella, C., Ceccarelli, C., et al. 2019, MNRAS, 483, 1850
Blake, G. A., Sutton, E. C., Masson, C. R., & Phillips, T. G. 1987, ApJ, 315, 621
Carrasco-González, C., Anglada, G., Rodríguez, L. F., Torrelles, J. M., & Osorio, M. 2008, AJ, 136, 2238
Ceccarelli, C. 2004, in ASP Conf. Ser. 323, The Hot Corinos of Solar Type Protostars, ed. D. Johnstone et al. (San Francisco, CA: ASP), 195
Ceccarelli, C., Maret, S., Tielens, A. G. G. M., Castets, A., & Caux, E. 2003, A&A, 410, 587
Codella, C., Ceccarelli, C., Cabrit, S., et al. 2016, A&A, 586, L3
Codella, C., Ceccarelli, C., Caselli, P., et al. 2017, A&A, 605, L3
Csengeri, T., Belloche, A., Bontemps, S., et al. 2019, A&A, 632, A57
de Jong, T., Boland, W., & Dalgarno, A. 1980, A&A, 91, 68
De Simone, M., Codella, C., Testi, L., et al. 2017, A&A, 599, A121
De Simone, M., Ceccarelli, C., Codella, C., et al. 2020, ApJL, 896, L3
Diaz-Rodriguez, A. K., Anglada, G., Blázquez-Calero, G., et al. 2021, arXiv:2111.11787
Dubernet, M.-L., Alexander, M. H., Ba, Y. A., et al. 2013, A&A, 553, A50
Endres, C. P., Drouin, B. J., Pearson, J. C., et al. 2009, A&A, 504, 635
Enrique-Romero, J., Ceccarelli, C., Rimola, A., et al. 2021, A&A, 655, A9
Enrique-Romero, J., Rimola, A., Ceccarelli, C., et al. 2019, ESC, 3, 2158
Enrique-Romero, J., Rimola, A., Ceccarelli, C., et al. 2022, ApJS, 259, 39
Ferrero, S., Zamirri, L., Ceccarelli, C., et al. 2020, ApJ, 904, 11
Flower, D. R., Pineau Des Forêts, G., & Walmsley, C. M. 2006, A&A, 449, 621
Frisch, M. J., Trucks, G. W., Schlegel, H. B., et al. 2016, Gaussian 16 Revision C.01, https://gaussian.com/citation/
Garufi, A., Podio, L., Codella, C., et al. 2022, A&A, 645, A145
Grimme, S., Antony, J., Ehrlich, S., & Krieg, H. 2010, JChPh, 132, 154104
Grimme, S., Ehrlich, S., & Goerigk, L. 2011, JCoCh, 32, 1456
Hariharan, P. C., & Pople, J. A. 1973, Theoret. Chim. Acta, 28, 213
Hehre, W. J., Ditchfield, R., & Pople, J. A. 1972, JChPh, 56, 2257
Hunter, J. D. 2007, CSE, 9, 90
Jørgensen, J. K., van der Wiel, M. H. D., Coutens, A., et al. 2016, A&A, 595, A117
Jørgensen, J. K., Müller, H. S. P., Calcutt, H., et al. 2018, A&A, 620, A170
Kleiner, I., Lovas, F. J., & Godefroid, M. 1996, JPCRD, 25, 1113
Krishnan, R., Binkley, J. S., Seeger, R., & Pople, J. A. 1980, JChPh, 72, 650
Kukolich, S. G., & Nelson, A. C. 1971, CPL, 11, 383
Lee, C., Yang, W., & Parr, R. G. 1988, PhRvB, 37, 785
Lefèvre, C., Cabrit, S., Maury, A. J., et al. 2017, A&A, 604, L1
Leurini, S., Schilke, P., Wyrowski, F., & Menten, K. M. 2007, A&A, 466, 215
López-Sepulcre, A., Jaber, A. A., Mendoza, E., et al. 2015, MNRAS, 449, 2438
López-Sepulcre, A., Sakai, N., Neri, R., et al. 2017, A&A, 606, A121
Manigand, S., Jørgensen, J. K., Calcutt, H., et al. 2020, A&A, 635, A48
Maret, S., Hily-Blant, P., Pety, J., Bardeau, S., & Reynier, E. 2011, A&A, 526, A47
McMullin, J. P., Waters, B., Schiebel, D., Young, W., & Golap, K. 2007, in ASP Conf. Ser. 376, CASA Architecture and Applications, ed. R. A. Shaw, F. Hill, & D. J. Bell (San Francisco, CA: ASP), 127
Milam, S. N., Savage, C., Brewster, M. A., Ziurys, L. M., & Wyckoff, S. 2005, ApJ, 634, 1126
Müller, H. S. P., Schlöder, F., Stutzki, J., & Winnewisser, G. 2005, JMoSt, 742, 215
Nazari, P., van Gelder, M. L., van Dishoeck, E. F., et al. 2021, A&A, 650, A150
Öberg, K. I., & Bergin, E. A. 2021, PhR, 893, 1
Ossenkopf, V., & Henning, T. 1994, A&A, 291, 943
Oya, Y., Sakai, N., Lefloch, B., et al. 2015, ApJ, 812, 59
Peng, T. C., Despois, D., Brouillet, N., et al. 2013, A&A, 554, A78
Pickett, H. M., Poynter, R. L., Cohen, E. A., et al. 1998, JQSRT, 60, 883
Pineda, J. E., Segura-Cox, D., Caselli, P., et al. 2020, NatAs, 4, 1158
Rabli, D., & Flower, D. R. 2010, MNRAS, 406, 95
Sakai, N., Sakai, T., Hirota, T., et al. 2014, Natur, 507, 78
Sakai, N., Oya, Y., Higuchi, A. E., et al. 2017, MNRAS, 467, L76
Segura-Cox, D. M., Schmiedeke, A., Pineda, J. E., et al. 2020, Natur, 586, 228
Sheehan, P. D., & Eisner, J. A. 2017, ApJ, 851, 45
Sheehan, P. D., Tobin, J. J., Federman, S., Megeath, S. T., & Looney, L. W. 2020, ApJ, 902, 141
Tobin, J. J., Looney, L. W., Li, Z.-Y., et al. 2016, ApJ, 818, 73
Tobin, J. J., Looney, L. W., Li, Z.-Y., et al. 2018, ApJ, 867, 43
van Gelder, M. L., Tabone, B., Tychoniec, Ł., et al. 2020, A&A, 639, A87
Xu, L.-H., & Lovas, F. J. 1997, JPCRD, 26, 17
Xu, L.-H., Fisher, J., Lees, R. M., et al. 2008, JMoSp, 251, 305
Yang, Y.-L., Sakai, N., Zhang, Y., et al. 2021, ApJ, 910, 20
Yen, H.-W., Gu, P.-G., Hirano, N., et al. 2019, ApJ, 880, 69